



**HAL**  
open science

## Mechanical Behaviour of the Rotating Target SORGENTINA-RF

Marco Lamberti, Ranieri Marinari, Andrea Mancini, Gianni Gadani, Antonino  
Pietropaolo

► **To cite this version:**

Marco Lamberti, Ranieri Marinari, Andrea Mancini, Gianni Gadani, Antonino Pietropaolo. Mechanical Behaviour of the Rotating Target SORGENTINA-RF. Applied Sciences, 2023, 13 (15), pp.8967. 10.3390/app13158967 . hal-04313934

**HAL Id: hal-04313934**

**<https://hal.science/hal-04313934>**

Submitted on 29 Nov 2023

**HAL** is a multi-disciplinary open access archive for the deposit and dissemination of scientific research documents, whether they are published or not. The documents may come from teaching and research institutions in France or abroad, or from public or private research centers.

L'archive ouverte pluridisciplinaire **HAL**, est destinée au dépôt et à la diffusion de documents scientifiques de niveau recherche, publiés ou non, émanant des établissements d'enseignement et de recherche français ou étrangers, des laboratoires publics ou privés.



Distributed under a Creative Commons Attribution 4.0 International License

# Mechanical Behaviour of the Rotating Target SORGENTINA-RF

Marco Lamberti <sup>1,2,\*</sup> , Ranieri Marinari <sup>3</sup> , Andrea Mancini <sup>3</sup>, Gianni Gadani <sup>3</sup>, Antonino Pietropaolo <sup>3</sup>   
and The SRF Collaboration <sup>†</sup>

<sup>1</sup> LMA, Aix-Marseille University, CNRS, Centrale Marseille, 13453 Marseille, France

<sup>2</sup> ENEA—Management of Infrastructures and Services, 00196 Rome, Italy

<sup>3</sup> ENEA—Department of Fusion and Technologies for Nuclear Safety and Security, 00196 Rome, Italy; ranieri.marinari@enea.it (R.M.); andrea.mancini@enea.it (A.M.); gianni.gadani@enea.it (G.G.); antonino.pietropaolo@enea.it (A.P.)

\* Correspondence: lamberti@lma.cnrs-mrs.fr or marco.lamberti@enea.it

<sup>†</sup> The SRF Collaboration: A list of authors and their affiliations appears in the acknowledgement section.

**Abstract:** The SORGENTINA-RF project aims at developing a 14 MeV neutron source based on a deuterium/tritium ion accelerator and a rotating target where fusion reactions take place. Among the different research fields, the most interesting and promising is medical radioisotope production. In this framework, intense research work on the design of the rotating target has been carried out. More in detail, to define the optimal design configuration, a sensitivity analysis on the mechanical performance of the rotating target considering the influence of some relevant parameters, such as material type, thickness, and presence of internal stiffeners, was carried out. Among the materials analyzed, aluminium alloy represents the best compromise to efficiently address all the critical requirements in the design phase. One of the most demanding project requirements that the conceptual design must fulfill is the ability of the target to dissipate a thermal power of 250 kW without precluding its mechanical properties and resistance. To investigate the performance of the rotating target, some thermo-mechanical analyses were undertaken with finite element method under some thermal transients and mechanical loads able to simulate the working conditions of the system. The numerical results emphasise the target's ability to withstand operating conditions. The main outcomes of the present study have been implemented as engineering solutions in the project design.

**Keywords:** thermal-mechanical analysis; finite element model; fusion; neutron source



check for updates

**Citation:** Lamberti, M.; Marinari, R.; Mancini, A.; Gadani, G.; Pietropaolo, A.; The SRF Collaboration.

Mechanical Behaviour of the Rotating Target SORGENTINA-RF. *Appl. Sci.* **2023**, *13*, 8967. <https://doi.org/10.3390/app13158967>

Academic Editor: Ana Martins Amaro

Received: 15 July 2023

Revised: 31 July 2023

Accepted: 2 August 2023

Published: 4 August 2023



**Copyright:** © 2023 by the authors. Licensee MDPI, Basel, Switzerland. This article is an open access article distributed under the terms and conditions of the Creative Commons Attribution (CC BY) license (<https://creativecommons.org/licenses/by/4.0/>).

## 1. Introduction

The SORGENTINA-RF project aims to develop a 14 MeV neutron source from deuterium-tritium fusion reactions with an expected power of 250 kW with the main purpose of producing medical radioisotopes as highlighted by some recent experimental evidence obtained at ENEA laboratories [1,2]. The neutron source is based on an ion source and accelerator which, from a gas of deuterium (D<sub>2</sub>) and tritium (T<sub>2</sub>), produce, extract, and accelerate D<sup>+</sup> and T<sup>+</sup> ions up to 300 keV against a rotating target fusion reactions occur thus producing 14 MeV neutrons.

In particular, the 14 MeV neutron source will be used to assess the production of <sup>99</sup>Mo as a precursor of <sup>99m</sup>Tc, widely used in medical diagnostics for SPECT (Single-Photon-Emission Computed Tomography).

The project represents a step towards a plant where relevant quantities of molybdenum can be irradiated and in turn radiochemical treatment at the same site. For its complexity, the project is divided into two main steps: in the first phase, the so-called thermo-mechanical demonstrator, composed of a rotating target equipped with the heat removal system and the ion source will be developed and tested separately; in the second, the ion source and the radiochemical facility for molybdenum treatment will be fully developed.

More in detail, the assembly depicted in Figure 1 is composed of the rotating target and its auxiliary components (i.e., vacuum chamber, reservoir, etc.). The rotating target has a double scope, allowing the implantation of deuterium and tritium into a thin titanium layer (about 3  $\mu\text{m}$ ) properly deposited on the target surface and dissipating the thermal power (250 kW) delivered by the accelerator.

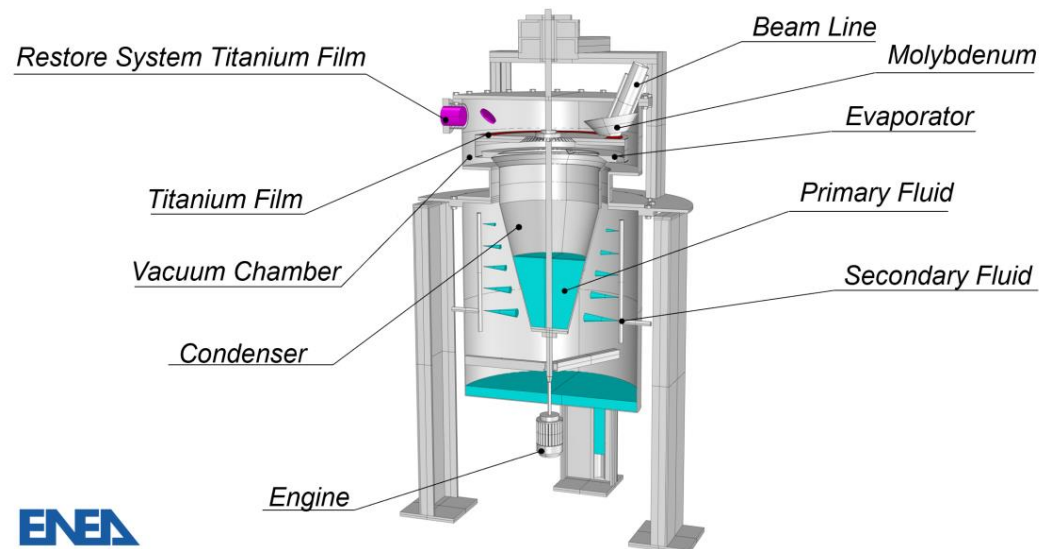


**Figure 1.** Thermo-mechanical demonstrator.

The heat source for the rotating target consists of an ion source (currently in a design stage) accelerating both deuterium and tritium against the external cylindrical surface of the rotating target. The colliding particles are collimated in a circular shape (150 mm in diameter) by the accelerating grids while the ion source is inclined by  $45^\circ$  on the vertical plane. This layout generates an elliptical footprint on the external surface of the rotating target. Regarding the homogeneity of the heat generated, the ion source will grant a  $\pm 10\%$  difference all over the impact surface that is simulated with a uniform heat flux boundary condition in the FEM analyses.

The rotating target is a prototypical out-of-scale rotating heat pipe (RHP) (Patent PCT/IB2019/051,972). The RHP mainly consists of three regions: the evaporator where a fluid is heated up (by the ion source) to its evaporation/boiling (in the upper region), a lower conical condenser region where the vapour previously generated finds a cold surface to condensate and then moves back to the evaporator thanks to the centrifugal effect of the rotation, an adiabatic region between the two previous ones where the condensate moves back to the evaporator.

The general description of the project and the main activities can be found in further detail in [3] while a set of specific studies is presented in [4–10].

In this paper, the methodology and main outcomes from the analysis for the design and optimisation of the prototype of the rotating target are discussed.

The rotating target can be essentially divided into three regions: the upper part, henceforth named the evaporator, the lower part, named the condenser connected to the external cooling system for heat removal, and the mid-region in between the two.

The Finite Element Method (FEM) was adopted to calculate the strength of the rotating target under complex load scenarios as the one foreseen during the functioning of the device. Several thermo-mechanical analyses were performed in order to investigate the mechanical performance of the target and the main numerical results are herein discussed. The temperature field, resulting from the energy deposition of  $\text{D}^+$  and  $\text{T}^+$  ions into the target and removed by the cooling system, has been evaluated in previous studies [6] and here used as input in FEM analyses. In addition, a sensitivity analysis to assess the

influence of some mechanical parameters on the behaviour of the rotating target is presented and discussed.

## 2. SORGENTINA RF Rotating Target

The thermo-mechanical demonstrator to be tested in the first phase of the project is the rotating target assembly shown in Figure 1. The outer side surface of the disk-shaped evaporator intercepts D<sup>+</sup> and T<sup>+</sup> 300 keV ions coming from the ion source. The evaporator has a perfectly cylindrical shape characterised by the major radius.

On the other hand, the condenser has a conical shape and is connected to the external water-cooling system. The whole scaled system, containing water, dissipates the power load due to the impinging ion beam by means of a heat transfer mechanism similar to a heat pipe system. The cooling fluid is at sub-atmospheric pressure due to its well-known properties in worldwide usage and experience as a coolant in power plants.

More in detail, the cooling system is designed to safely remove a thermal power of 250 kW concentrated over a circular hot spot of about 150 mm in diameter, and thus an average heat flux of about 14 MW/m<sup>2</sup>.

The concept of the target cooling system was oriented to a rotating component working with a closed and localised thermal cycle to avoid any external hazard. The cooling fluid selected is water at sub-atmospheric pressure due to its well-known properties in the literature and worldwide usage and experience as a coolant in power plants.

The cooling system identified is a prototypical out-of-scale rotating heat pipe (RHP) [11–13]. The RHP mainly consists of three regions: the evaporator where a fluid is heated up to its evaporation/boiling, a conical condenser region where the vapour previously generated finds a cold surface to condensate and then moves towards the evaporator thanks to the centrifugal effect of the rotation, an adiabatic region between the two previous ones where the condensate moves back to the evaporator (Figure 1).

In between the evaporator and condenser, vacuum seals and bearings are located allowing the machine operation.

The geometrical dimensions of the structures are here summarised: the total height is 2400 mm, the diameter of the evaporator is 1000 mm, and the diameter of the condenser varies from 200 to 400 mm.

Working conditions foresee the target rotating at a constant speed under irradiation of 833 mA (total electric current) of deuterons and tritons ions at 300 keV, thus releasing a thermal power of 250 kW in the target. Thermal power deposited by alpha particles into the target from fusion reactions is negligible (<100 W). The area enlightened by the ion beam is circular, with a diameter of about 100–120 mm. The thermal power deposited onto the target surface diffuses into the device through conduction and represents the main potential cause of system failure. The frequency rotation of the rotating target is equal to 5.3 Hertz. A schematic representation of the rotating target and the intercepted ion beam is depicted in Figure 2.

As can be seen from Figure 2 the ion beam is inclined with respect to the external surface of the evaporator. Due to the projection onto it, the footprint of the ion beam (150 mm) is different from its diameter (about 100–120 mm).

### 2.1. Influence of Design Parameters

The influence of some design parameters (type of material, thickness, presence of internal stiffeners) on the mechanical performance of the assembly has been investigated to optimise the design, guarantee the required performance, and ensure adequate robustness of the device. Such analysis allowed us to address the present design as well as optimise the geometrical and mechanical properties of the structures.

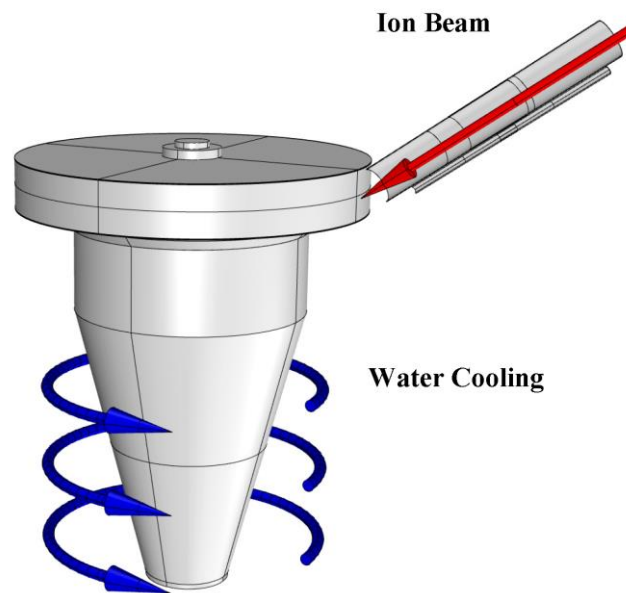


**Figure 2.** Rotating target system (3D View).

## 2.2. Material

Four metal alloys, listed in Table 1, were considered in order to fulfil the strict performance requirements described in [3]: titanium (Ti), aluminium (Al), copper–chromium–zirconium (CuCrZr), and tungsten (W). It is worth underlining that the metal alloy has to guarantee the following characteristics:

- High thermal conductivity;
- Low neutron activation in order to minimise the production of radioactive waste;
- Good mechanical properties;
- Good chemical compatibility with water.

**Table 1.** Mechanical properties of metallic alloys selected for parametric study.

| Material | $\lambda$<br>[W/(m K)] | $\alpha$<br>[C <sup>-1</sup> ] | $r$<br>[kg/m <sup>3</sup> ] | $c$<br>[J/(kg K)] | $E$<br>[MPa] | $\sigma_y$<br>[MPa] |
|----------|------------------------|--------------------------------|-----------------------------|-------------------|--------------|---------------------|
| Al       | 174                    | $2.35 \times 10^{-5}$          | $2.69 \times 10^3$          | 921               | 69,000       | 250                 |
| CuCrZr   | 318                    | $1.67 \times 10^{-5}$          | $8.90 \times 10^3$          | 376               | 127,500      | 220                 |
| W        | 90                     | $5.00 \times 10^{-6}$          | $1.85 \times 10^4$          | 134               | 385,000      | 800                 |
| Ti       | 17                     | $8.5 \times 10^{-6}$           | $4.40 \times 10^3$          | 544               | 110,000      | 800                 |

The mechanical properties of these alloys are summarised in Table 1, where the symbol  $\lambda$  denotes the thermal conductivity,  $\alpha$  the linear expansion coefficient,  $r$  the mass density,  $c$  the specific heat capacity,  $E$  the Young's Modulus, and  $\sigma_y$  the yield strength.

The mechanical properties reported in Table 1 allow us to make some considerations: tungsten has good mechanical properties (i.e., provides a high value of yield strength and high Young's Modulus) being a very resistant and low deformable material. On the contrary, it is characterised by relatively poor thermal properties in terms of conductive heat transfer due to the low value of linear expansion coefficient and low thermal conductivity. Moreover, the high density would make the system heavier concerning the other materials.

Similar considerations can be assumed for the titanium alloy that provides a high value of high strength and good deformability, but poor thermal conductivity.

Differently, aluminium and copper–chromium–zirconium alloys provide lower yield strength, but good deformability and higher value of thermal conductivity.

To evaluate the materials' performance concerning thermal distortion, a simple case was considered, i.e., an element of the structure with a non-uniform power deposition. This

was modelled as a fixed-ended beam subject to a non-uniform thermal distortion with a rectangular section as shown in Figure 3.

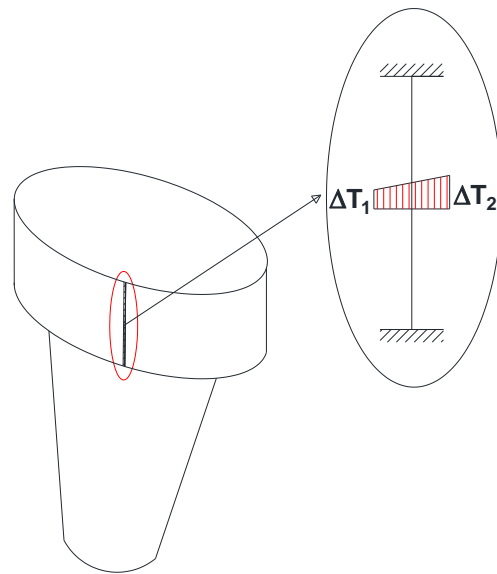


**Figure 3.** Schematic representation of the effects of power deposition by means of a fixed-ended beam subject to a non-uniform thermal distortion.

Being that the element is hyperstatic, it is possible to calculate the maximum stress due to the presence of thermal loads as reported in Equation (1). In this equation, the symbol  $\Delta T_{m1}$  represents the temperature load that produces linear deformation while the symbol  $\Delta T_{m2}$  is the temperature load that produces flexural deformation,  $h$  represents the height of the beam, and  $y$  the distance from the centroid. The results for any material were expressed in terms of normalised strength obtained by dividing the yield strength of each metallic alloy for the stress calculated using Equation (1), assuming a thermal gradient of 30 °C from the external to the internal side of the evaporator [6]. The results are summarised in Figure 4. It is important to underline, that the normalised strength is expressed in percentage and represents the fraction of the strength of the material used to withstand the expected loads due to the presence of a non-uniform thermal distortion.

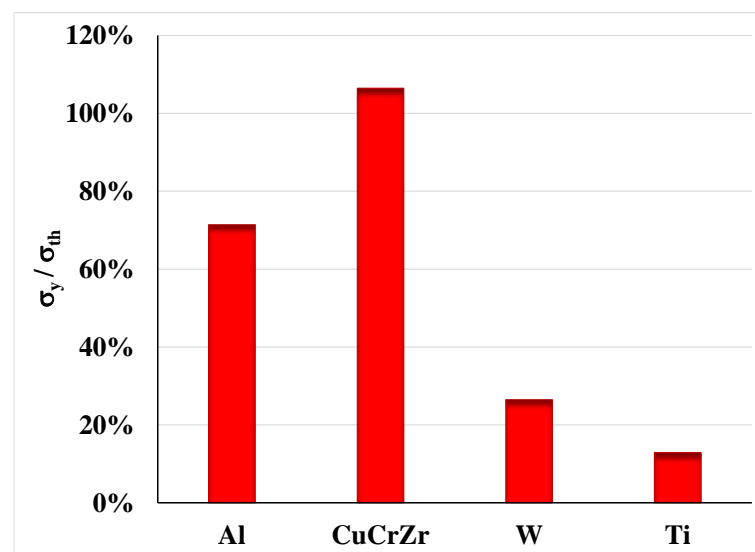


**Figure 4.** Normalised strength value for different materials.

The evaluation of  $\Delta T_{m1}$  and  $\Delta T_{m2}$  are reported in Equation (2):

$$\sigma_{\Delta T} = E \left( \alpha \Delta T_{m1} + \frac{2\alpha \Delta T_{m2}}{h} y \right) \quad (1)$$

$$\Delta T_{m1} = \frac{\Delta T_1 + \Delta T_2}{2} \quad (2a)$$

$$\Delta T_{m2} = \frac{\Delta T_2 - \Delta T_1}{2} \quad (2b)$$

As shown in Figure 4, the stress due to the thermal effect for CuCrZr exceeds its yield strength being the normalised strength equal to 106%.

Titanium is the material that provides the lowest value of the normalised strength with a value of 13%, also exhibiting a considerable resistance (high value of yield strength). Aluminium alloy provides a value of 71%, meaning that the strength capacity of material subject to the conditions considered is largely exploited but is still capable of withstanding increased stresses due to applied forces.

A high value of yield strength is an important requirement that the structure has to fulfil, but is not the only parameter to consider in the choice of material. Although tungsten and titanium alloys provide the highest resistance and stiffness, their low thermal conductivity cannot be neglected, as it could compromise the correct operation of the system.

Furthermore, standard materials such as the CuCrZr alloy show high material activation, and titanium alloy, which could be a candidate, has a high permeability to tritium. Using FISPACT-II code the dose trend of different materials after 1 year of exposure of 1 kg at 1 m distance from the ion source has been quantified [14]. More in detail, the number of D + T particles onto the target considering 200 days/year is about  $9 \times 10^{25}$  particles in one activity year. Because of the low D and T energy (300 keV), these are completely stopped by the titanium layer of the target. The main effect on the Ti layer is physical sputtering. It is, indeed, foreseen that a Ti deposition plant, as described in [3], can be used to recover the sputtered Ti layer. Finally, the charged particle beam is not a concern for dpa. As far as neutron-induced dpa is concerned, the neutron emission rate is in the range of  $5\text{--}7 \times 10^{13} \text{ s}^{-1}$ . This emission rate may induce a fraction of dpa in aluminium. Thus, over 200 days/year, the dpa on the target is not detrimental. As a matter of fact, over a typical lifetime of the target (2–3 years) no primary beam neutron-induced thermal property changes are likely to occur.

The aluminum alloy showed the lowest material activation as reported in Figure 5.

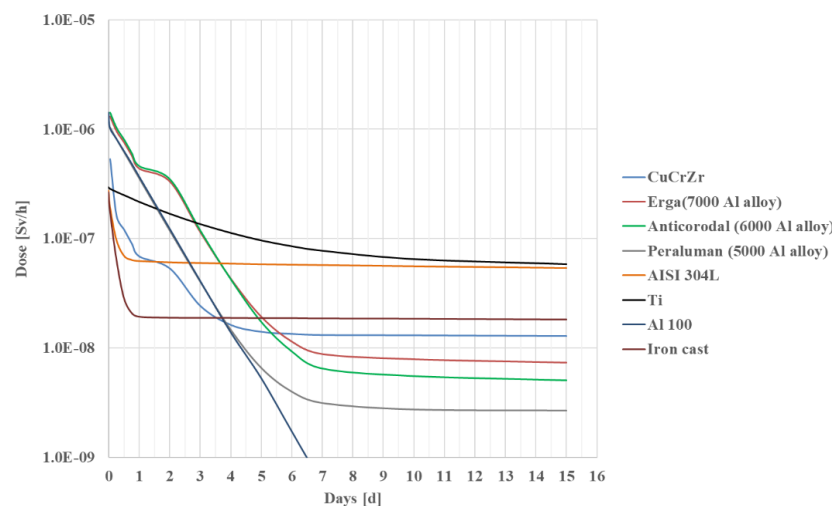


**Figure 5.** Dose trend of different materials after 1 year of exposure of 1 kg at 1 m distance from the ion source (FISPACT-II code results) [14].

On the other hand, the aluminium alloy exhibited good mechanical resistance, thermal conductivity, and chemical compatibility with water [4]. Aluminium alloy has many further advantages, such as lower cost, light density, good heat dissipation, recyclability, and low neutron activation.

For these reasons, aluminium alloy represents the best compromise to fulfil the above criteria and therefore is the most promising candidate as the material for the rotating target. In fact, thanks to its mechanical properties, it represents the best compromise between the required performance criteria: thermal exchange, mechanical strength, and low neutron activation.

### 2.3. Thickness

The choice of the thickness of the device represents an important issue. In fact, the wall has to be thin enough to guarantee a sufficiently large heat exchange and, at the same time, it should be thick enough to provide adequate stiffness and inertia of the structure to avoid the onset of instability phenomena.

Heat pipes have a working fluid kept at sub-atmospheric pressure. In this way, a pressure of around  $10^{-3}$  bar is imposed inside the rotating target. Outside, the presence of the cooling system and the atmospheric pressure generate a force due to the pressure gradient across the system's wall. Due to the pressure gradient between the external and internal environment of the structure, the critical pressure of instability [15] was calculated for several realistic thicknesses. In this way, it was possible to define the smallest thickness of the rotating target able to counteract the instability phenomena.

The critical pressure of instability can be evaluated by means of

$$p_{cr} = \frac{E}{4(1-\nu^2)} \left( \frac{t}{R} \right)^3 \quad (3)$$

where  $E$  and  $\nu$  are the Young and Poisson moduli, respectively,  $t$  is the thickness, and  $R$  is the radius.

Figure 6 shows the ratio of the critical pressure of instability to the gradient generated, as a function of the structural thickness, for the maximum radius of the conical condenser equal to  $R = 150$  and  $250$  mm, respectively. The variation of radius along the height of the condenser is accounted for.

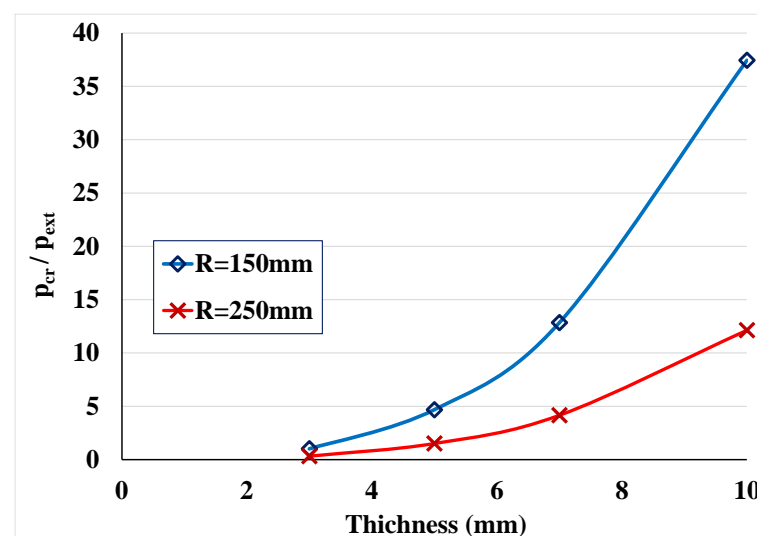


Figure 6. Normalised pressure of instability for different wall thicknesses.

The two curves represent an upper and lower limit within which it is possible to find a suitable solution. The wall was sized between 7 and 10 mm thick, in turn obtaining a

reasonable safety coefficient and offering a good contribution to the rigidity and resistance of the system.

Moreover, it has been demonstrated that the strength of the structure can counteract the circumferential and radial stress evaluated through the analytical formulas relative to the elastic problem of geometrically axial-symmetric solids of cylindrical shape, subject to external loads.

### 3. FEM Model of the Rotating Target

The mechanical behavior of the rotating target was investigated using a commercial FEM [16] software package [17]. The material properties assigned to the model are summarised in Table 1 and an isotropic behavior of the structural material was assumed.

In the model, off-plane displacements were inhibited on the lower, upper, and middle surfaces, thus reproducing the presence of shaft, seals, and bearings.

Four-node thermally coupled tetrahedron, linear displacement, and temperature elements named C3D4T were chosen to build the mesh. After element type and average size, a mesh with more than 3 million (3,054,114) elements with a maximum length of 8 mm, able to ensure the accuracy of results, was built and employed for the calculations. The 3D model for the target is shown in Figure 7.

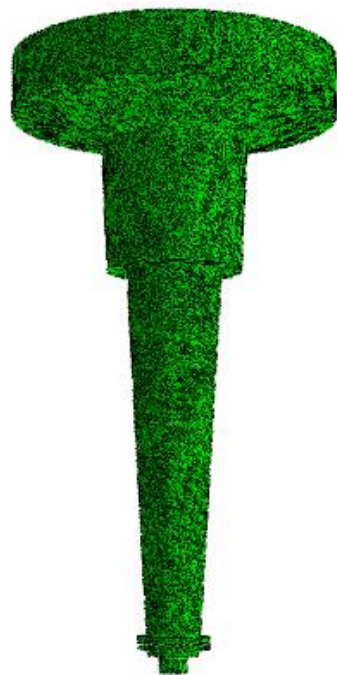


Figure 7. Target Mesh details.

In the following section, the external field force and boundary conditions have been described in detail.

#### 3.1. Boundary Conditions

The rotating target, during its operation, is subject to different types of actions: centrifugal force, pressure gradient, and variable thermal load.

However, due to the presence of the ion beam, the following temperature field was analytically and numerically estimated on the surface of the target [6] taking into account:

- presence of boiling water inside the device with a saturation temperature of 50 °C;
- working pressure inside the component of 0.1 bar;
- boiling water heat transfer coefficient (analytically estimated with Rohsenow correlation [18]) of about 18,165 W/m<sup>2</sup>/K;
- target thickness of 10 mm of aluminum alloy in the evaporator region;

- the density of the aluminum is to  $2.7 \text{ g/cm}^3$ , the thermal conductivity of the aluminum alloy is to  $170 \text{ W/m/K}$ , and the heat capacity of the material is equal to  $900 \text{ J/kg/K}$ ;

Thanks to all these assumptions, a transient RANS thermal–hydraulic simulation was performed on the heated region of the rotating target [6] to highlight the periodic temperature profile on the external surface of the evaporator to adopt as BC for the mechanical simulations. The time step selected for the simulation grants a Courant number lower than 1 (0.82) for the stability of the numerical simulation. The contour plot of the thermal field on the external surface of the rotating target is reported in Figure 8; the maximum temperature, about  $135 \text{ }^\circ\text{C}$ , was located in the area exposed to the beam spot while a kind of “comet effect” was highlighted downstream of it thanks to the cooling effect of the boiling water inside. The cold spot of about  $98 \text{ }^\circ\text{C}$  was located at the opposite side just upstream of the beam footprint.

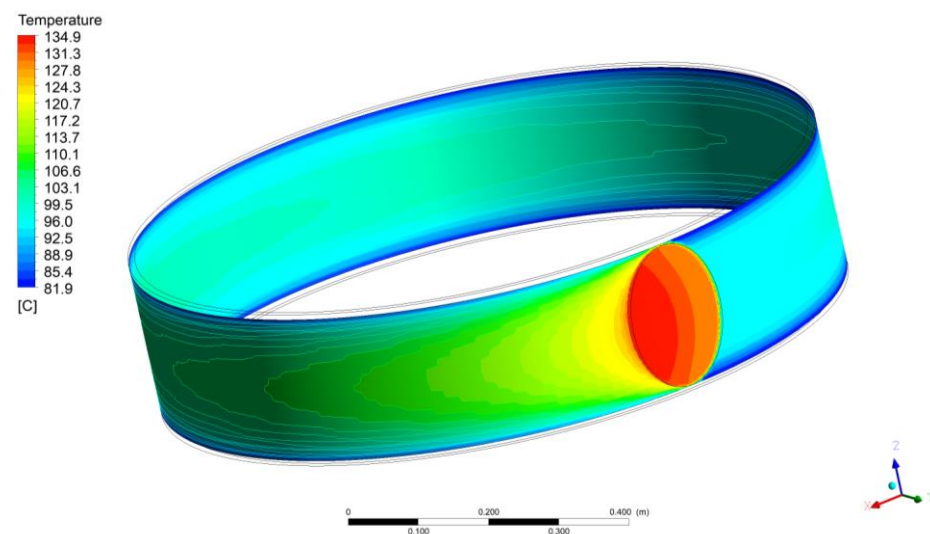


**Figure 8.** Temperature distribution on the lateral surface of the rotating target [6].

Thanks to these assumptions, the following boundary conditions were fixed for the FEM analyses:

- the temperature in the zone of incidence of the ion beam  $T = 135 \text{ }^\circ\text{C}$ ;
- the temperature on the rotating disc  $T = 100 \text{ }^\circ\text{C}$ ;
- the evaporator’s internal temperature  $T = 50 \text{ }^\circ\text{C}$ ;
- the internal condenser’s temperature  $T = 20 \text{ }^\circ\text{C}$ .

The rotating target during its operation rotates at a constant angular speed of  $33.15 \text{ rad/s}$ . Further assumptions were (1) the absence of pressure inside, (2) the presence of standard atmospheric pressure outside, and (3) the self-weight of the structure.

Once the model, nominal loads, and boundary conditions were defined, the mechanical performance of the device was investigated.

A couple of temperature-displacement procedures were implemented. The thermo-mechanical analysis allows a nonlinear calculation in which the mechanical stress and temperatures are solved iteratively accounting for the reciprocal action of the temperature on the stress and vice-versa.

Steady-state thermal analysis for evaluating the temperature at the thermal equilibrium of the system on the surface where subject to constant heat loads and environmental conditions over time was set.

The impinging ion beam source was modelled as a surface heat flux and was applied on the external surface of the evaporator.

A cylindrical coordinate system was adopted to consider the rotation of the target concerning the ion beam and to define the variable impact area:

$$x_{cord} = R \cos(\vartheta) \quad (4a)$$

$$y_{cord} = R \sin(\vartheta) \quad (4b)$$

$$Z_{cord} = Z_{center} \quad (4c)$$

where  $R$  is the radius of the evaporator,  $\vartheta$  the angle defined by the angular velocity and time, and  $Z_{center}$  is the coordinate along the vertical axis of the center of the circular impact area.

A subroutine was implemented in the FEM software to define the dimension of the area where the thermal power is deposited by the ion beam source.

### 3.2. Numerical Investigations on the Presence of Internal Stiffeners

The influence of internal stiffeners (inserted inside the evaporator) on the mechanical behaviour of the rotating target, subject to the actions listed in Section 3.1, was evaluated by means of FEM (finite element method) analysis.

Two configurations of evaporator were investigated: the first was characterised by the absence of internal stiffeners, case (a), as depicted in Figure 9a, and the second one by their presence, case (b), as depicted in Figure 9b.

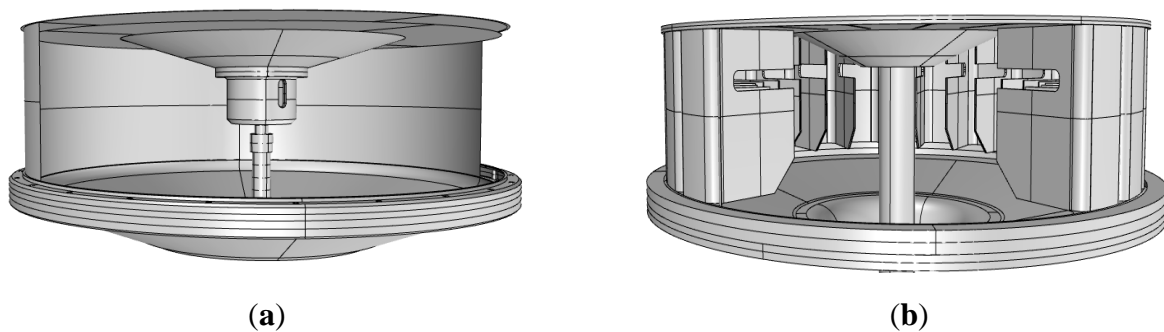


**Figure 9.** Internal view of the evaporator: (a) absence of internal stiffeners; (b) presence of internal stiffeners.

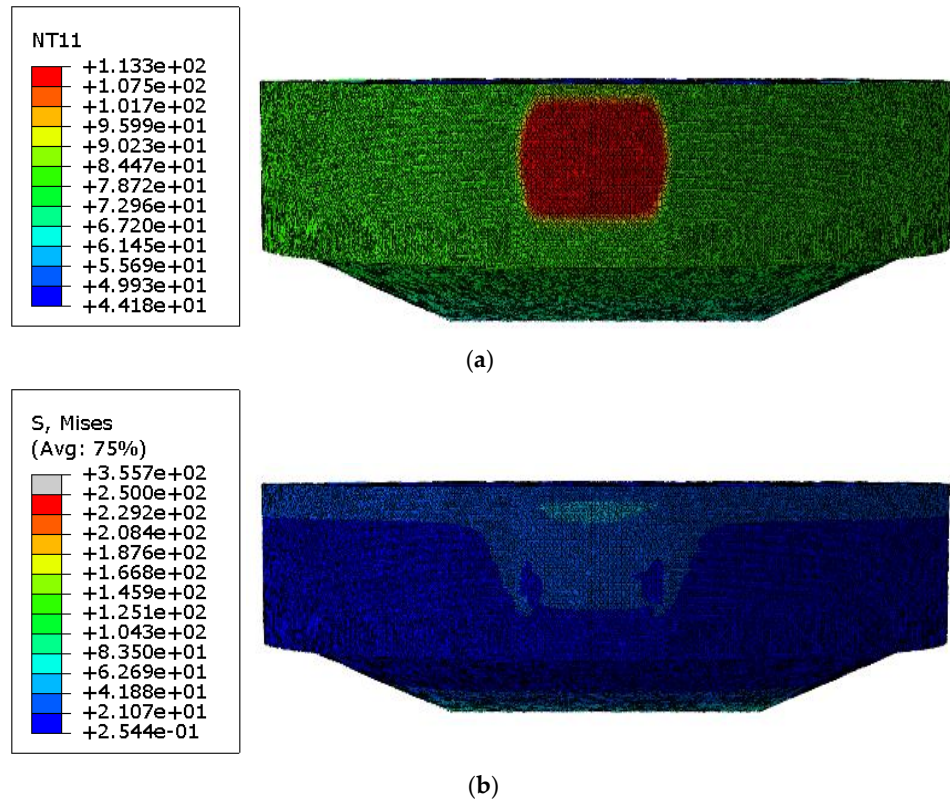
The internal stiffeners had a rectangular shape with dimensions of 190 mm width, 225 mm height, and 5 mm thickness. The internal stiffeners were placed every  $15^\circ$  for a total of 24 elements. Furthermore, the presence of an internal hole is due to fluid dynamics.

Figure 10 shows numerical results for the configuration without internal stiffeners. In particular, Figure 10a shows the temperature field, while Figure 10b the von Mises stress distribution, respectively.

Figure 10a shows the hot spot due to the ion beam power deposition (supposed uniform) where the maximum temperature reached was  $113^\circ\text{C}$ . The temperature moving towards the condenser was significantly lower due to the presence of the cooling system.

The von Mises criteria [19] were adopted to define the higher value of stress equal to 62 MPa inside the impact area of the evaporator.

In Figure 11a,b, the same calculations are reported for the case of an evaporator with internal stiffeners. Differently from the previous case, the temperature field does not appear uniform over the ion beam impact area (Figure 10a) but assumes higher values in correspondence with the internal stiffeners' positions.



**Figure 10.** (a) Temperature field in °C on the evaporator, case (a) without internal stiffeners. (b) Von Mises stress field in MPa of the evaporator, case (a) without internal stiffeners.

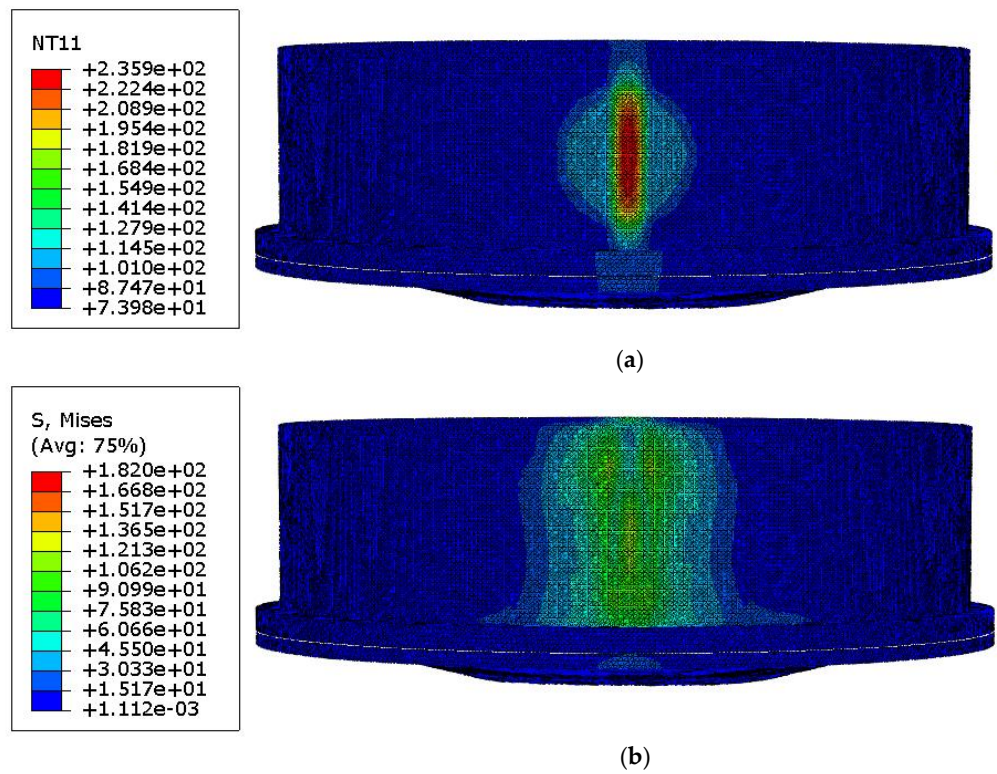


**Figure 11.** (a) Temperature field in °C on the evaporator, case (b) with internal stiffeners. (b) Von Mises stress field in MPa of the evaporator, case (b) with internal stiffeners.

The temperature field reached the highest value of 236 °C in the proximity of stiffeners. In the region between two stiffeners, under the application of ion beam thermal load, the temperature assumed a lower value, equal to 113 °C. Following the von Mises stress criteria, the maximum stress reached was 120 MPa. The internal stiffeners were anchored to the mantle of the evaporator, therefore representing a constraint that limits the possibility of displacements. As a consequence, the increment of temperatures and mechanical stress occurred in correspondence with stiffeners.

In Figure 12, the comparison of the temperature field between the two cases was made in terms of temperature under the hot spot for the two analysed typologies and for a different number of cycles. Each cycle represents a complete rotation of the target.

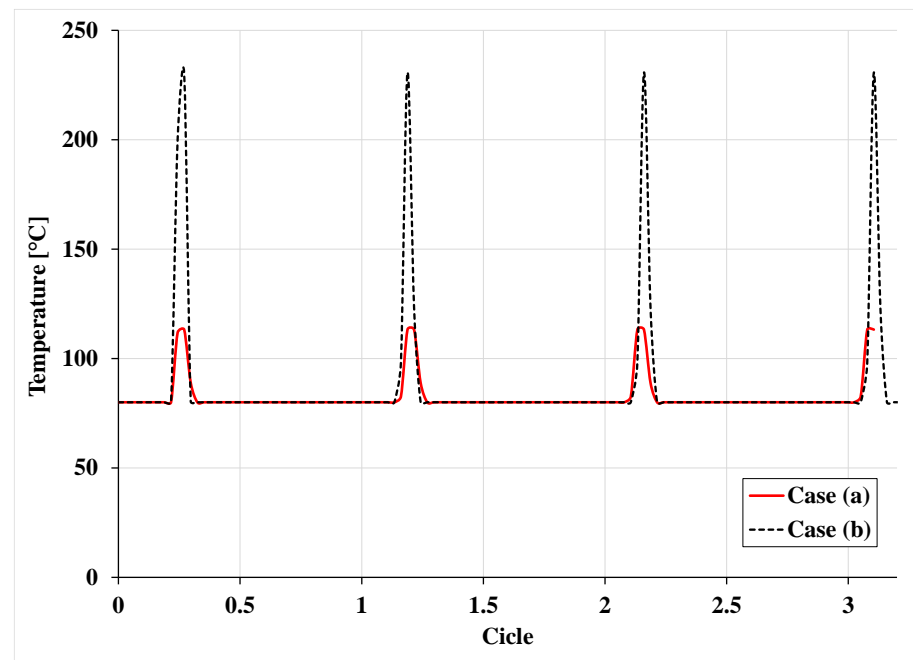


**Figure 12.** Comparison in terms of the temperature for case (a) and case (b) for the different number of cycles.

As already explained, the presence of internal stiffeners, provides hyperstatic constraints on the lateral mantle, thus also producing a higher temperature rise, when the surface is hit by the ion beam. The larger increase in temperature is due to the inability of the surface to freely deform out of the plane. On the other hand, the presence of internal stiffeners for their geometrical dimension increases the inertia in the plane leading to an improvement of the rigidity of the system and thus enhancing the instability safety factor.

In case (a), the temperature increase occurred when the reference point of the outer shell of the evaporator passed under the ion beam. However, this phenomenon is much less relevant concerning the previous case.

Figure 13 shows the comparison in terms of von Mises stresses as a function of the number of cycles for the two cases considered. Under the hot spot, a sudden increment of stress was recorded for both cases, but it was more evident in the system equipped with stiffeners.

In both configurations presented, the stress field did not exceed the strength yield limit of the material (Figure 13). It is important to underline that the current comparison has the only scope to provide a qualitative definition of the von Mises stress in both configurations.

The high operational temperature can provoke a reduction of the strength of the material with time (ageing) and therefore have a severe effect on the lifetime of the component.

The latter aspect led to considering the rotating target without stiffeners as the best solution.

It is important to point out that the presence of the other external forces does not represent a particular concern from a mechanical resistance point of view.

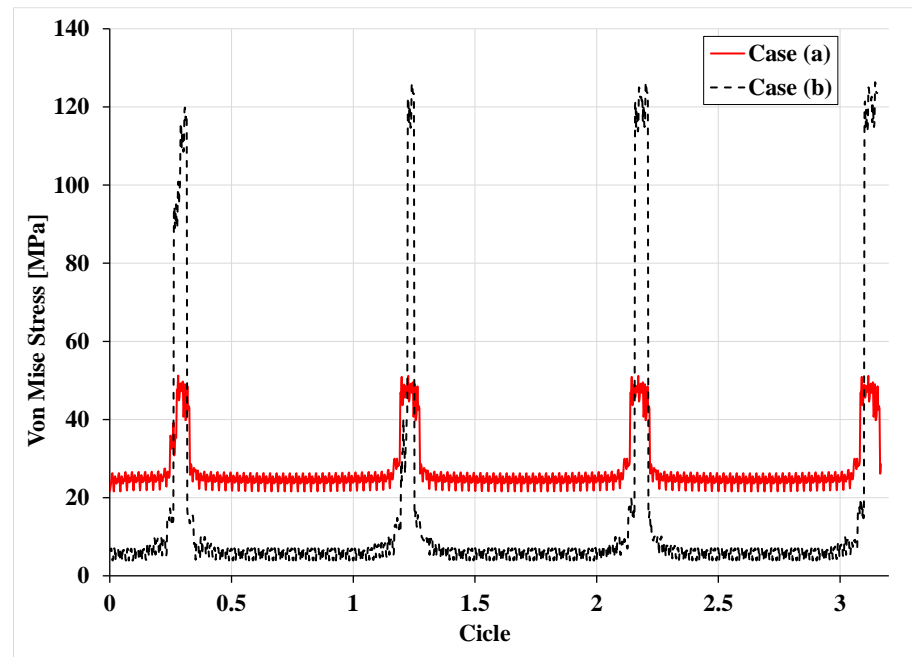


Figure 13. Comparison in terms of von Mises stresses for case (a) and case (b) for the different number of cycles.

### 3.3. Numerical Investigations on Rotating Target

Boundary and load conditions previously described were implemented in the FEM model for studying the thermo-mechanical behaviour of the target.

In Figure 14, the temperature field on the target surface is reported. The upper region of the target is characterised by higher values of temperature. The temperature decreased towards the condenser region due to the presence of the external cooling system.

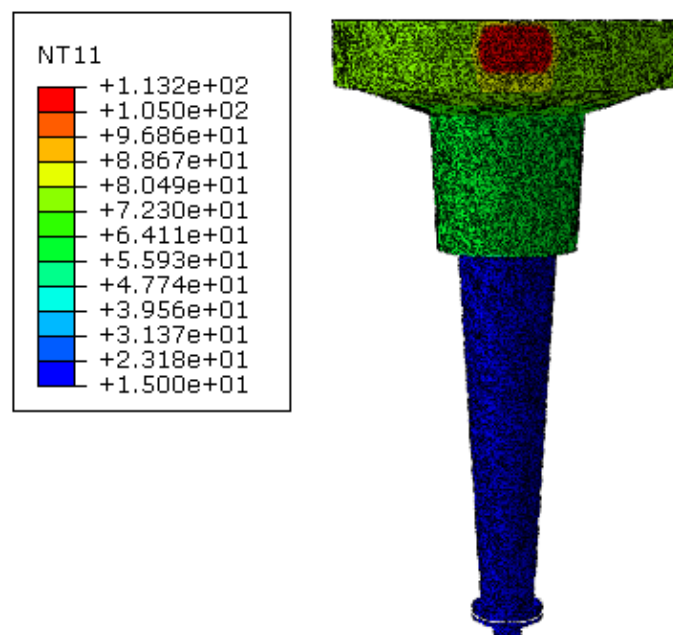


Figure 14. Target temperature field in °C.

The Von Mises stress map is given in Figure 15. Higher mechanical stress is in the central region between the evaporator and the condenser (maximum is 111 MPa), with a corresponding temperature of 62 °C.

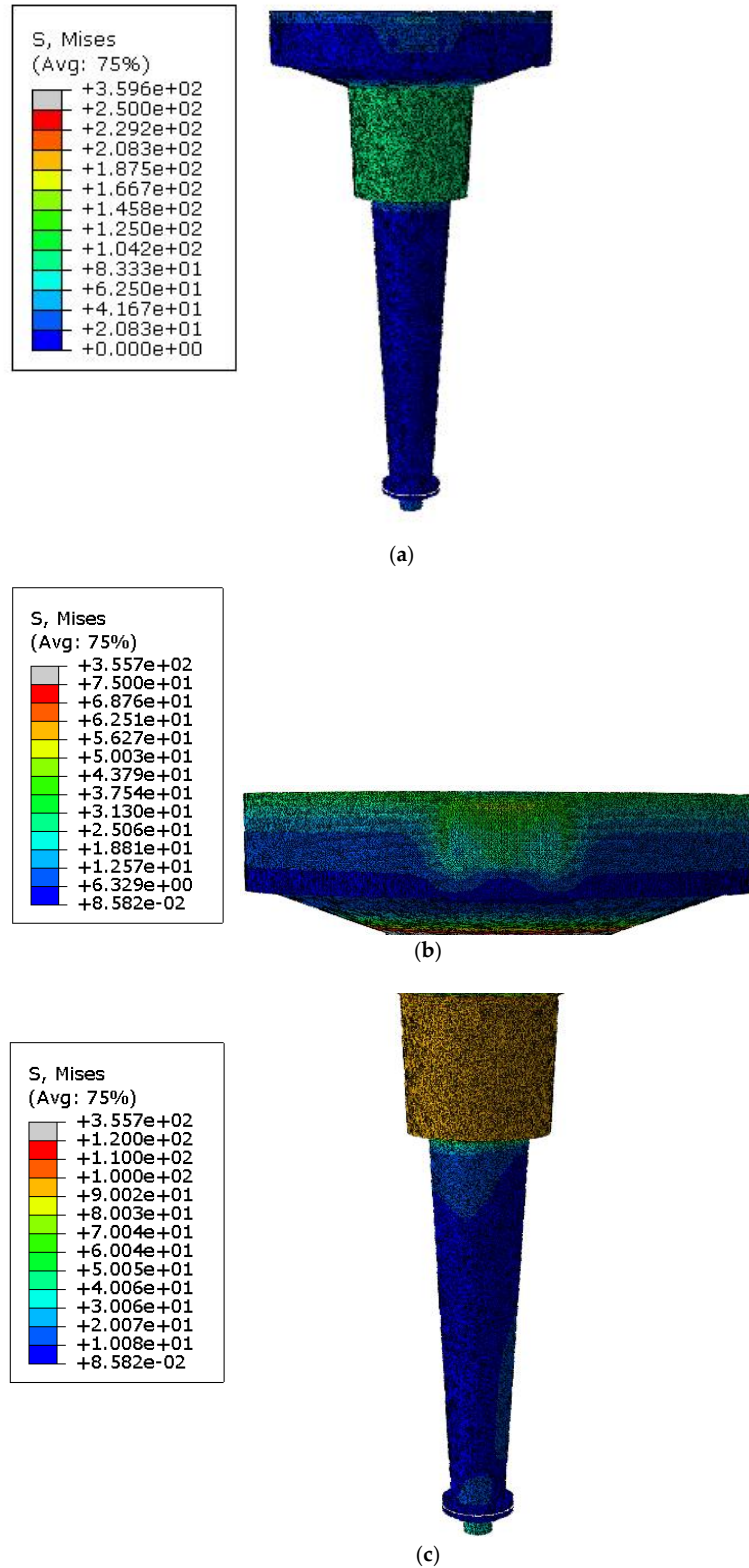


Figure 15. (a) Von Mises stress distribution in MPa. (b) Von Mises stress distribution in MPa (detail of the evaporator). (c) Von Mises stress distribution in MPa (detail of the condenser).

Moreover, it can be clearly observed that the maximum von Mises stress in the target surface did not exceed the yield strength of the material, and thus the global structural integrity is assured. Furthermore, the conical structure was chosen to reduce thermal effects.

Furthermore, the presence of cyclic thermal stresses due to temperature changes can lead to the failure of the rotating target following the formation of macroscopic cracks [20]. Thermal fatigue may occur also without mechanical loads. The cracks, in fact, could develop after many cycles of heating and cooling. For this reason, thermal fatigue life represents the major issue for the lifetime of the target.

An estimation of the fatigue effect can be carried out by comparing the stress amplitude with the allowable limit.

The allowable limit is often proportional to the material strength. The proportionality factor for metal and alloy is in the range of 0.35 and 0.5 [21]. The allowable limit turns out to be equal to around 90 MPa. On the other hand, from the numerical simulation performed, the stress amplitude results are equal to 14.85 MPa in the region of the evaporator (Figure 13). From the comparison, the stress amplitude is lower than the fatigue limit for a safety coefficient of about 5.

Finally, in Figure 16, the displacement field is shown: the maximum displacement reached was 1.164 mm, in the evaporator region. Lower displacements were exhibited in the condenser.

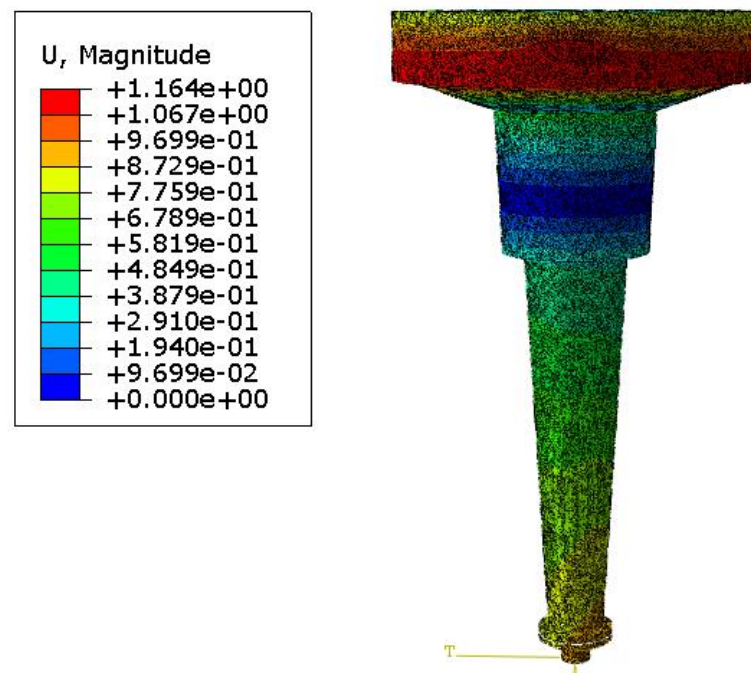


Figure 16. Displacement distribution map in mm.

#### 4. Conclusions

Within the framework of project SORGENTINA-RF, some preliminary mechanical assessment of the performance of the rotating target was carried out. The influence of some design parameters (type of material, thickness, presence of internal stiffeners) on the mechanical performance of the assembly was investigated to optimise the design and to guarantee the required performance and ensure adequate robustness of the device to optimise the design and allow the fulfilment of the thermal and mechanical requirements.

The numerical results support the following conclusions:

- (1) Among the materials analyzed, aluminium alloy represents the best compromise to efficiently address the critical requirements;

- (2) The von Mises stress distribution on the evaporator surface was lower in the configuration without internal stiffeners;
- (3) The rotating target design responded efficiently to the external force field.

The current state of the design seems the most appropriate among the many configurations studied so far. Further numerical analysis will be performed, and experimental tests will be undertaken to validate the models so far employed in the design phase. In particular, the experimental tests will focus attention on the effects of temperatures and thermal cycles during a year of operation on the material's mechanical properties.

**Author Contributions:** Conceptualization, M.L., R.M., A.M., G.G. and A.P.; methodology, M.L.; software, M.L.; formal analysis, M.L.; validation M.L.; investigation, M.L.; data curation, M.L.; writing—original draft preparation, M.L.; writing—review and editing, all the author, project administration, A.P. All authors have read and agreed to the published version of the manuscript.

**Funding:** This research received no external funding.

**Institutional Review Board Statement:** Not applicable.

**Informed Consent Statement:** Not applicable.

**Data Availability Statement:** The datasets generated during and/or analyzed during the current study are not publicly available due to patent but are available from the corresponding author upon reasonable request.

**Acknowledgments:** The authors acknowledge the Regione Emilia Romagna-ENEA agreement for the project "SORGENTINA RF-Thermomechanical Demonstration". <sup>†</sup>The SRF Collaboration: Pietro Agostini (ENEA-Department of Fusion and Technologies for Nuclear Safety and Security, 00196 Rome, Italy), Massimo Angiolini (ENEA-Department of Fusion and Technologies for Nuclear Safety and Security, 00196 Rome, Italy), Ciro Alberghi (University of Turin, 10124 Turin, Italy), Marco Capogni (ENEA-Department of Fusion and Technologies for Nuclear Safety and Security, 00196 Rome, Italy; ENEA—Italian National Institute of Ionizing Radiation Metrology, Italy), Mauro Capone (ENEA-Department of Fusion and Technologies for Nuclear Safety and Security, 00196 Rome, Italy; ENEA—Italian National Institute of Ionizing Radiation Metrology, Italy), Sebastiano Cataldo (ENEA-Department of Fusion and Technologies for Nuclear Safety and Security, 00196 Rome, Italy), Gian Marco Contessa (ENEA-Department of Fusion and Technologies for Nuclear Safety and Security, 00196 Rome, Italy), Francesco D'Annibale (ENEA—Department Energy Technologies and Renewable Sources, 00196 Rome, Italy), Marco D'Arienzo (ASL Roma 6, Borgo Garibaldi, 12, 00041 Albano Laziale (RM), Italy), Dario Diamanti (ENEA-Department of Fusion and Technologies for Nuclear Safety and Security, 00196 Rome, Italy), Danilo Dongiovanni (ENEA-Department of Fusion and Technologies for Nuclear Safety and Security, 00196 Rome, Italy), Mirko Farini (ENEA-Management of Infrastructures and Services, 00196 Rome, Italy), Paolo Ferrari (ENEA—Institute of Radiation Protection, 00196 Rome, Italy), Angela Fiore (ENEA-Department of Fusion and Technologies for Nuclear Safety and Security, 00196 Rome, Italy), Davide Flammini (ENEA-Department of Fusion and Technologies for Nuclear Safety and Security, 00196 Rome, Italy), Manuela Frisoni (ENEA-Department of Fusion and Technologies for Nuclear Safety and Security, 00196 Rome, Italy), Nicola Fonnese (ENEA-Department of Fusion and Technologies for Nuclear Safety and Security, 00196 Rome, Italy), Angelo Gentili (ENEA—Department Energy Technologies and Renewable Sources, 00196 Rome, Italy), Giacomo Grasso (ENEA-Department of Fusion and Technologies for Nuclear Safety and Security, 00196 Rome, Italy), Manuela Guardati (ENEA—Institute of Radiation Protection, 00196 Rome, Italy), David Guidoni (ENEA-Management of Infrastructures and Services, 00196 Rome, Italy), Luigi Lepore (ENEA-Department of Fusion and Technologies for Nuclear Safety and Security, 00196 Rome, Italy), Andrea Mariani (ENEA—Department Energy Technologies and Renewable Sources, 00196 Rome, Italy), Giuseppe A. Marzo (ENEA-Department of Fusion and Technologies for Nuclear Safety and Security, 00196 Rome, Italy), Bruno Mastroianni (ENEA-Management of Infrastructures and Services, 00196 Rome, Italy), Fabio Moro (ENEA-Department of Fusion and Technologies for Nuclear Safety and Security, 00196 Rome, Italy), Agostina Orefice (ENEA-Department of Fusion and Technologies for Nuclear Safety and Security, 00196 Rome, Italy), Tonio Pinna (ENEA-Department of Fusion and Technologies for Nuclear Safety and Security, 00196 Rome, Italy), Antonietta Rizzo (ENEA-Department of Fusion and Technologies for Nuclear Safety and Security, 00196 Rome, Italy), Alexander Rydzy (ENEA-Department of Fusion and Technologies for Nuclear Safety and Security, 00196 Rome, Italy),

Stefano Salvi (ENEA-Department of Fusion and Technologies for Nuclear Safety and Security, 00196 Rome, Italy), Demis Santoli (ENEA-Department of Fusion and Technologies for Nuclear Safety and Security, 00196 Rome, Italy), Alessia Santucci (ENEA-Department of Fusion and Technologies for Nuclear Safety and Security, 00196 Rome, Italy), Luca Saraceno (ENEA—Department Energy Technologies and Renewable Sources, 00196 Rome, Italy), Camillo Sartorio (ENEA-Department of Fusion and Technologies for Nuclear Safety and Security, 00196 Rome, Italy), Valerio Sermenghi (ENEA-Department of Fusion and Technologies for Nuclear Safety and Security, 00196 Rome, Italy), Emanuele Serra (ENEA—Department for Sustainability, 00196 Rome, Italy), Salvatore Scaglione (ENEA—Department Energy Technologies and Renewable Sources, 00196 Rome, Italy), Andrea Simonetti (ENEA-Department of Fusion and Technologies for Nuclear Safety and Security, 00196 Rome, Italy), Ivan Panov Spassovsky (ENEA-Department of Fusion and Technologies for Nuclear Safety and Security, 00196 Rome, Italy), Nicholas Terranova (ENEA-Department of Fusion and Technologies for Nuclear Safety and Security, 00196 Rome, Italy), Silvano Tosti (ENEA-Department of Fusion and Technologies for Nuclear Safety and Security, 00196 Rome, Italy), Alberto Ubaldini (ENEA-Department of Fusion and Technologies for Nuclear Safety and Security, 00196 Rome, Italy), Marco Utili (ENEA-Department of Fusion and Technologies for Nuclear Safety and Security, 00196 Rome, Italy), Konstantina Voukelatou (ENEA-Department of Fusion and Technologies for Nuclear Safety and Security, 00196 Rome, Italy), Pietro Zito (ENEA-Department of Fusion and Technologies for Nuclear Safety and Security, 00196 Rome, Italy), Danilo Zola (ENEA—Department Energy Technologies and Renewable Sources, 00196 Rome, Italy), Giuseppe Zummo (ENEA—Department Energy Technologies and Renewable Sources, 00196 Rome, Italy).

**Conflicts of Interest:** The authors declare no conflict of interest.

## References

1. Capogni, M.; Pietropaolo, A.; Quintieri, L.; Angelone, M.; Boschi, A.; Capone, M.; Cherubini, N.; De Felice, P.; Dodaro, A.; Duatti, A.; et al. 14 MeV Neutrons for  $^{99}\text{Mo}/^{99\text{m}}\text{Tc}$  Production: Experiments, Simulations and Perspectives. *Molecules* **2018**, *23*, 1872. [CrossRef] [PubMed]
2. Capogni, M.; Pietropaolo, A.; Quinteri, L. RT/2016/32/ENEA. 2016. Available online: <https://iris.enea.it/retrieve/dd11e37c-d7ba-5d97-e053-d805fe0a6f04/RT-2016-32-ENEA.pdf> (accessed on 14 July 2023).
3. Pietropaolo, A.; Contessa, G.M.; Farini, M.; Fomesu, N.; Marinari, R.; Moro, F.; Rizzo, A.; Scaglione, S.; Terranova, N.; Utili, M.; et al. SORAGENTINA-RF project: Fusion neutrons for  $^{99}\text{Mo}$  medical radioisotope. *Eur. Phys. J. Plus* **2021**, *136*, 1140. [CrossRef]
4. Sartorio, C.; Angiolini, M.; Flammini, D.; Pietropaolo, A.; Agostini, P.; Alberghi, C.; Candido, L.; Capogni, M.; Capone, M.; Cataldo, S.; et al. Preliminary Assessment of Radiolysis for the Cooling Water System in the Rotating Target of SORAGENTINA-RF. *Environments* **2022**, *9*, 106. [CrossRef]
5. Ferrari, P.; Contessa, G.M.; Moro, F.; Gadani, G.; Lepore, L.; Pietropaolo, A.; Agostini, P.; Angiolini, M.; Alberghi, C.; Candido, L.; et al. Sorentina-RF Fusion Neutron Plant: Preliminary Design of the Bioshielding in Compliance with Dose Constraints for Workers Exposure. *Radiat. Prot. Dosim.* **2022**, *198*, 1409–1416. [CrossRef] [PubMed]
6. Marinari, R.; Lamberti, M.; Agostini, P.; Del Nevo, N.; Mancini, A.; Pietropaolo, A.; Gadani, G. Thermal hydraulic design of a heat removal system for a fusion accelerator. In Proceedings of the 20th International Topical Meeting on Nuclear Reactor Thermal Hydraulics (NURETH-20), Washington, DC, USA, 20–25 August 2023.
7. Fomesu, N.; Scaglione, S.; Spassovsky, I.P.; Pietropaolo, A.; Zito, P.; Agostini, P.; Angiolini, M.; Alberghi, C.; Candido, L.; Capogni, M.; et al. On the definition of the deuterium-tritium ion beam parameters for the SORAGENTINA-RF fusion neutron source. *Eur. Phys. J. Plus* **2022**, *137*, 1150. [CrossRef]
8. Fomesu, N.; Scaglione, S.; Spassovsky, I.P.; Zito, P.; Pietropaolo, A.; Agostini, P.; Angiolini, M.; Alberghi, C.; Candido, L.; Capogni, M.; et al. On the expected performance of the SORAGENTINA-RF fusion neutron source. *Eur. Phys. J. Plus* **2022**, *137*, 1240. [CrossRef]
9. Contessa, G.M.; Terranova, N.; Pinna, T.; Dongiovanni, D.N.; D'arienzo, M.; Moro, F.; Ferrari, P.; Pietropaolo, A.; The SRF Collaboration. Risk Management of a Fusion Facility: Radiation Protection and Safety Integrated Approach for the Sorentina-RF Project. *Environments* **2022**, *9*, 71. [CrossRef]
10. Cicconi, F.; Ubaldini, A.; Fiore, A.; Rizzo, A.; Cataldo, S.; Agostini, P.; Pietropaolo, A.; Salvi, S.; Cuzzola, V.; on behalf of the SRF Collaboration. Dissolution of Molybdenum in Hydrogen Peroxide: A Thermodynamic, Kinetic and Microscopic Study of a Green Process for  $^{99\text{m}}\text{Tc}$  Production. *Molecules* **2023**, *28*, 2090. [CrossRef] [PubMed]
11. Faghri, A. Heat Pipes and Thermosyphons. In *Handbook of Thermal Science and Engineering*; Kulacki, F., Ed.; Springer: Cham, Switzerland, 2017. [CrossRef]
12. Faghri, A. Heat Pipes: Review, Opportunities And Challenges. *Front. Heat Pipes* **2014**, *5*, 1–48. [CrossRef]
13. Song, F.; Ewing, D.; Ching, C. Fluid flow and heat transfer model for high-speed rotating heat pipes. *Int. J. Heat Mass Transf.* **2003**, *46*, 4393–4401. [CrossRef]

14. Frisoni, M. *Private Communications on FISPACT Software Results*; ENEA–Department of Fusion and Technologies for Nuclear Safety and Security: Rome, Italy, 2022.
15. Wang, W.; Cai, G.; Zhou, J. Large-scale Vacuum Vessel Design and Finite Element Analysis. *Chin. J. Aeronaut.* **2012**, *25*, 189–197. [[CrossRef](#)]
16. Camprini, P.C.; Bernardi, D.; Pillon, M.; Angelone, M.; Frisoni, M.; Pietropaolo, A.; Pizzuto, A.; Agostini, P. Design optimization and performances of New Sorgentina Fusion Source (NSFS) supporting materials research. *Fusion Eng. Des.* **2015**, *96–97*, 236–239. [[CrossRef](#)]
17. Michael, S. *ABAQUS/Standard Use's Manual, Version 6.9*; Dassault Systèmes Simulia Corp: Providence, RI, USA, 2009.
18. Rohsenow, W.M. A Method of Correlating Heat-Transfer Data for Surface Boiling of Liquids. *J. Fluids Eng.* **1952**, *74*, 969–975. [[CrossRef](#)]
19. ASME Section VIII Division 1: Boiler and Pressure Vessel Code (BPVC). Available online: <https://www.asme.org/codes-standards/find-codes-standards/bpvc-viii-1-bpvc-section-viii-rules-construction-pressure-vessels-division-1/2023/print-book> (accessed on 14 July 2023).
20. Qianfan, X. Durability and reliability in diesel engine system design. In *Diesel Engine System Design*; Elsevier: Amsterdam, The Netherlands, 2013.
21. Militky, J.; Ibrahim, S. Effect of textile processing on fatigue. In *Fatigue Failure of Textile Fibres*; Woodhead Publishing Series in Textiles: Sawston, CA, USA, 2009; pp. 133–168.

**Disclaimer/Publisher's Note:** The statements, opinions and data contained in all publications are solely those of the individual author(s) and contributor(s) and not of MDPI and/or the editor(s). MDPI and/or the editor(s) disclaim responsibility for any injury to people or property resulting from any ideas, methods, instructions or products referred to in the content.